Ion-exchange assisted charge storage via strategic intercalation of $ZnCo_2O_4/V_2O_5$ heterostructures for high-energy hybrid supercapacitors

Mehedi Hasan[1], Md. Raihan Siddiki[2], Md. Abdullah Zubair[2] and Muhammad Rakibul Islam[1]*
*Department of Physics, Bangladesh University of Engineering and Technology (BUET), Dhaka-1000, Bangladesh.
[2]Department of Nanomaterials and Ceramics Engineering, Bangladesh University of Engineering and Technology (BUET), Dhaka-1000, Bangladesh.
*Email: rakibul@phy.buet.ac.bd

Electronic Supporting Information (ESI)

Note S1. Synthesis method

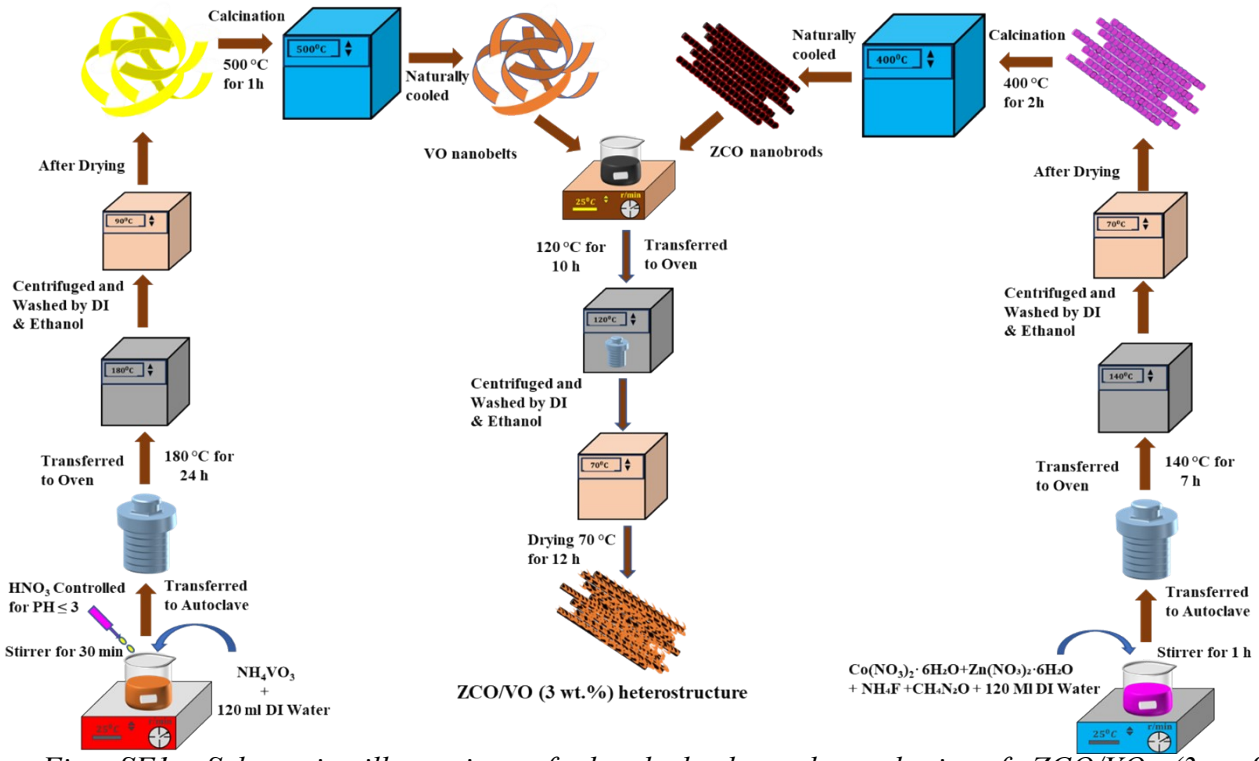

Fig. SF1: Schematic illustration of the hydrothermal synthesis of ZCO/VO (3 wt%) nanocomposites. ZCO nanorods were obtained via hydrothermal treatment of the precursor solution, followed by drying and calcination at 500 °C. Separately, VO precursors were treated hydrothermally, dried, and calcined at 400 °C to form VO nanobelts. The two components were then combined through a hydrothermal process, dried, and calcined to yield the ZCO/VO (3 wt%) nanocomposite. The same protocol was employed for the preparation of ZCO/VO (5 wt%) and ZCO/VO (7 wt%) nanocomposites.

Note S2. Electrochemical characterizations:

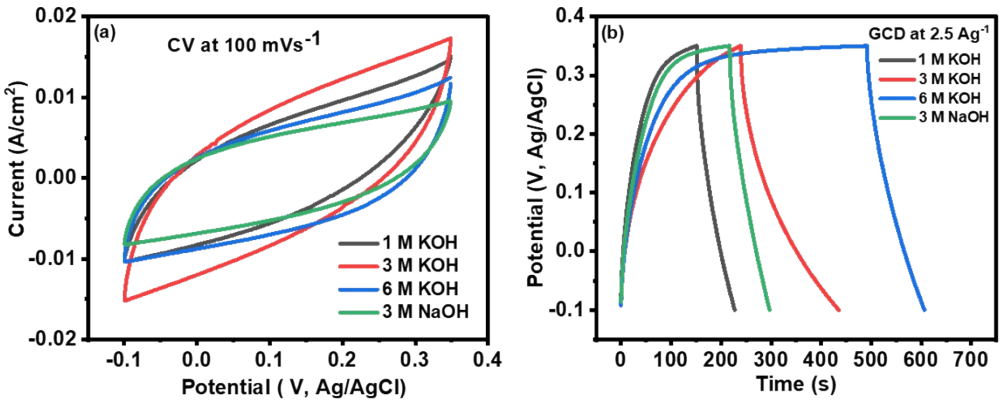

Fig. SF2. (a) CV curves and (b) GCD profiles of the ZCO/VO electrode measured in different electrolytes (1, 3, and 6 M KOH, and 3 M NaOH), demonstrating the superior electrochemical performance in 3 M KOH.

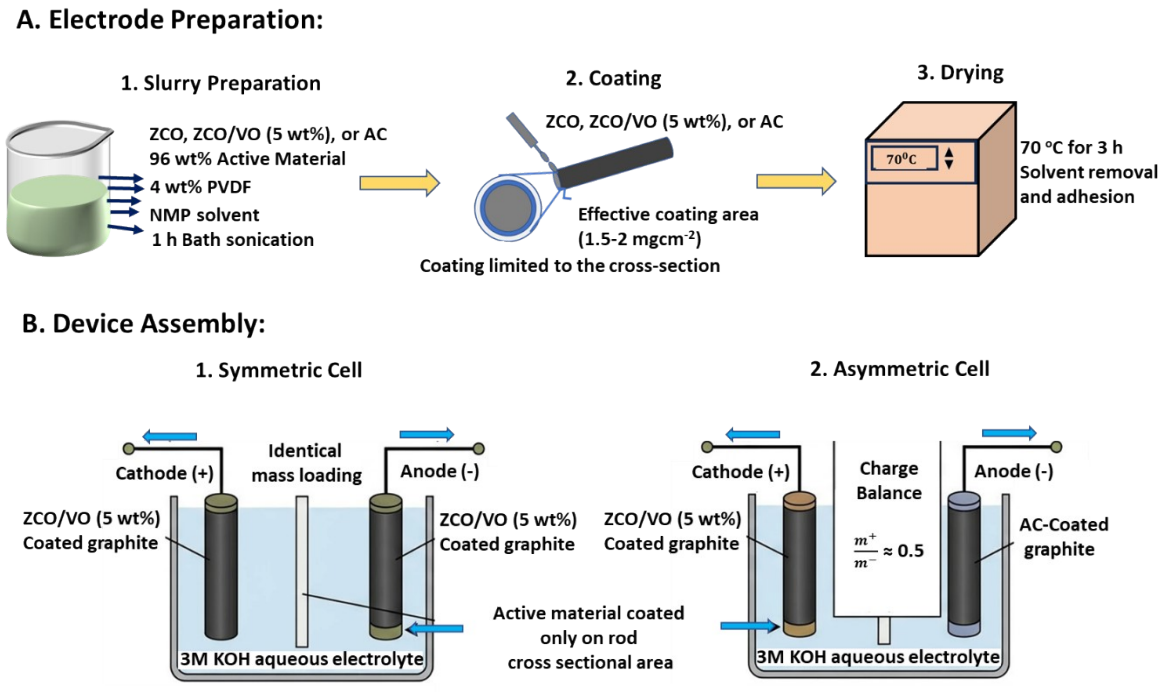

Fig. SF3: Schematic diagram of the device assembly process, including electrode slurry preparation, coating on graphite substrates, and thermal drying. The configurations used for electrochemical testing are illustrated, showing the placement of the cathode, anode, separator, and the 3 M KOH aqueous electrolyte. Both the symmetric cell (identical mass loading on both electrodes) and the asymmetric ZCO/VO//AC device with charge-balanced electrodes are depicted.

Note S3. Scanning Electron Microscopy (SEM)

a. Diameter and length distribution curve of ZCO, VO, and ZCO/VO (5 wt%) nanocomposite:

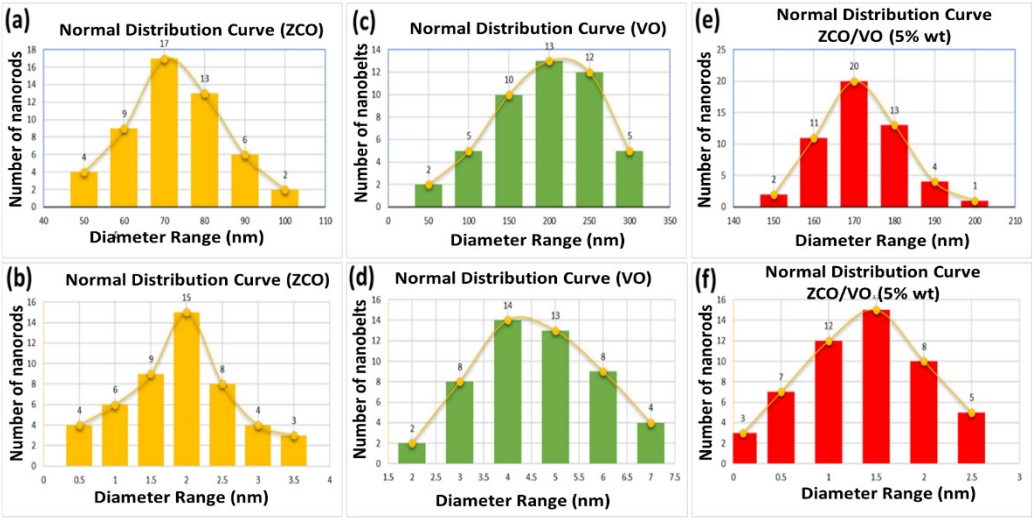

Fig. SF4: Diameter and length distribution histograms of ZCO, VO, and ZCO/VO (5 wt%) nanobelts derived from SEM images. The distributions were evaluated using ImageJ software. (a,b) Diameter and length distribution of ZCO nanorods, showing sizes in the range of 50–100 nm and 0.5–3.5 µm, respectively. (c,d) Diameter and length distribution of VO nanobelts, with values ranging from 50–300 nm and 2.0–7.0 µm, respectively. (e,f) Diameter and length distribution of ZCO/VO (5 wt%) nanocomposites, exhibiting diameters of 150–200 nm and lengths of 0.1–2.5 µm.

b. Porosity Analysis:

Table ST-1: The porosity values of ZCO and ZCO/VO heterostructures were determined using MATLAB [S(1,2)].

Sample	Porosity (%)	Average Pore Radius (nm)	Standard Deviation of Pore radius(nm)
ZCO	17.8	16.5751	13.318
VO	10.8	16.016	18.136
ZCO/VO (3 wt%)	6.45	15.727	15.583
ZCO/VO (5 wt%)	6.43	10.149	11.651
ZCO/VO (7 wt%)	6.58	13.023	13.639

As shown in Table ST-1, the ZCO/VO (5 wt%) heterostructure exhibits the highest porosity (0.658%) and the smallest average pore radius (10.149 nm), indicating a more compact structure with increased free volume. Conversely, the ZCO/VO (7 wt%) nanocomposite displays a gradual decrease in porosity (0.643%), suggesting greater structural relaxation at elevated VO content.

c. Energy Dispersive X-ray Analysis (EDX)

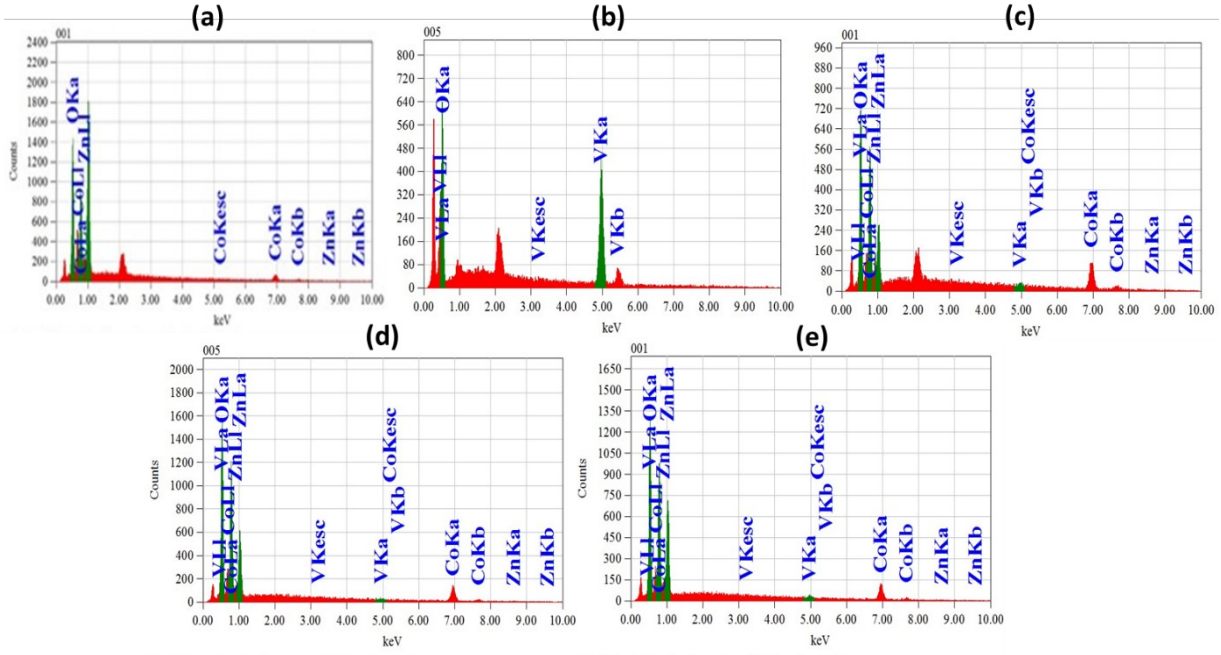

Fig. SF5: EDX spectra of (a) ZCO nanorods with hierarchically assembled nanopetals, (b) VO nanobelt nanoparticles, (c) ZCO/VO (3 wt%), (d) ZCO/VO (5 wt%), and (e) ZCO/VO (7 wt%) nanocomposites. The spectra were collected from randomly chosen regions of each sample and clearly identified Zn, Co, and O in ZCO; V and O in VO; and Zn, Co, V, and O in all ZCO/VO nanocomposites. The absence of additional peaks confirms the high phase purity of the materials without any detectable elemental contamination.

Table ST-2: Elemental composition (%) from EDX spectra of ZCO, VO, and ZCO/VO heterostructures

Sample	Zn	Co	V	O
ZCO	23.15	24.74	-	52.11
VO	-	-	47.80	52.20
ZCO/ VO (3 wt%)	6.80	36.54	1.70	54.97
ZCO/ VO (5 wt%)	8.39	36.28	0.68	54.70
ZCO/ VO (7 wt%)	11.84	34.67	0.96	52.53

As shown in Table ST-2, the slight decrease in the measured vanadium atomic percentage at higher VO loading can be attributed to the surface-sensitive and semi-quantitative nature of EDX analysis. Since EDX probes only a localized surface region, the detected elemental ratios may not fully represent the bulk composition. At higher VO concentrations, vanadium oxide may form layered or aggregated domains on the ZCO surface, leading to local compositional variations within the analyzed region. Consequently, the stronger contribution from Zn and Co signals of the underlying ZCO framework can influence the normalized EDX atomic percentages, resulting in an apparent reduction in the measured vanadium content.

Note S4. Transmission Electron Microscopy (TEM)

Selected area electron diffraction (SAED) analysis:

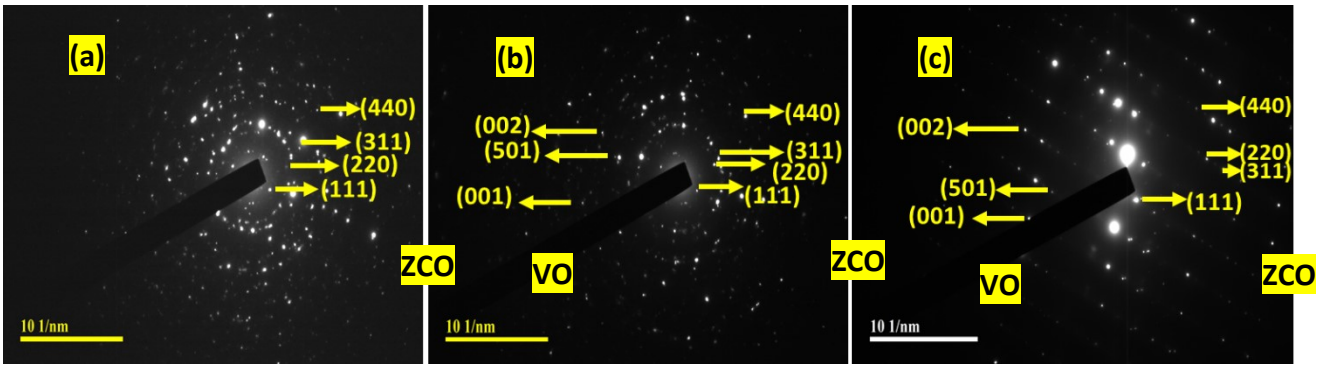

Fig. SF6. SAED patterns of (a) ZCO, (b) ZCO/VO (3 wt%), and (c) ZCO/VO (7 wt%) nanostructures. The well-defined diffraction rings and bright spots correspond to the (111), (220), (311), and (440) planes of cubic ZCO and the (001), (002), and (501) planes of VO, consistent with the XRD results. The presence of distinct and sharp diffraction rings confirms the polycrystalline nature and high crystallinity of the ZCO/VO heterostructures.

Note S5. X-ray Diffraction (XRD):

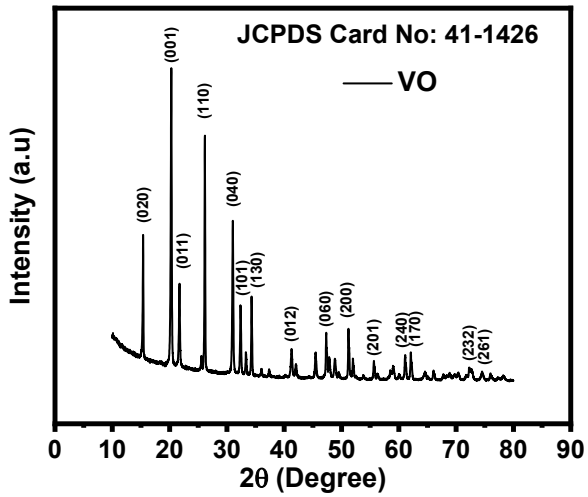

Fig. SF7. XRD pattern of VO nanostructures, showing diffraction peaks indexed to the (001), (020), (110), (021), (111), (200), (131), (002), (220), (202), (221), (132), and (231) planes, in good agreement with the standard JCPDS card No. 41-1426. The sharp and well-defined peaks confirm the crystalline nature of the synthesized VO.

Table ST-3: Crystallinity values of ZCO and ZCO/VO nanocomposites at different VO loadings, calculated from XRD analysis.

Sample	Crystallinity (%)	d-spacing from XRD (311) plane (nm)	d-spacing from TEM (311) plane (nm)
ZCO	74.89	0.240	0.23
ZCO/VO (3 wt%)	86.80	0.249	0.25
ZCO/VO (5 wt%)	94.24	0.250	0.28
ZCO/VO (7 wt%)	75.57	0.244	0.24

The crystallinity values from XRD (Table ST3) show that ZCO has 74.89% crystallinity, which increases to 86.80% and 94.24% for ZCO/VO (3 wt%) and ZCO/VO (5 wt%), respectively. This improvement can be ascribed to the synergistic interaction between ZCO and VO, which enhances structural ordering. However, at higher VO loading (7 wt%), the crystallinity decreases to 75.57%, likely due to lattice strain and agglomeration, suggesting that 5 wt% VO provides the optimum crystallinity for improved electrochemical performance.

Sample	Element	Oxidation State	Peak Position (eV)	Area (a.u.)	Fraction (%)
ZCO	Co 2p	Co^{3+}	~779.6–780.2	224.11	65.0
		Co^{2+}	~781.0–782.3	120.68	35.0
ZCO/VO (5%)	Co 2p	Co^{3+}	~779.8–780.5	213.77	62.0
		Co^{2+}	~781.2–782.5	131.02	38.0
ZCO/VO (5%)	V 2p	V^{5+}	~517.2	85.28	72.0
		V^{4+}	~516.2	33.16	28.0

Note S6. X-ray Photoelectron Spectroscopy (XPS):

Table ST-4. Quantitative XPS analysis of Co 2p and V 2p spectra, including binding energies, integrated peak areas, and the calculated relative content ratios of Co^{2+}/Co^{3+} and V^{4+}/V^{5+} oxidation states.

A quantitative analysis of the Co 2p and V 2p XPS spectra was performed by integrating the fitted peak areas, and the results are summarized in Table ST-4. The ZCO sample shows a dominant Co^{3+} contribution (65.0%) compared to Co^{2+} (35.0%), while the ZCO/VO (5%) nanocomposite

exhibits a slight increase in Co^{2+} content (38.0%), indicating modulation of the cobalt valence state. Additionally, the coexistence of V^{5+} (72.0%) and V^{4+} (28.0%) confirms the presence of mixed valence vanadium species.

This mixed valence state distribution is closely associated with the enhanced electrochemical performance, as it provides multiple redox-active sites and facilitates improved charge transfer kinetics, thereby leading to enhanced pseudocapacitive behaviour and rate capability.

Table ST-5: Deconvolution results of the O 1s spectra for ZCO and ZCO/VO (5 wt%), highlighting the enhanced oxygen vacancy fraction after VO incorporation.

Sample	Component	Center (eV)	Sigma (eV)	Area (a.u.)	Fraction (O_V/O_L) (%)
ZCO	Lattice O_L (O^{2-})	529.387	0.4636	210000.5264	0.38
ZCO	Defect/O_V (~531 eV)	531.243	0.7256	80858.84162	
ZCO	OH/Adsorbed (~532.5 eV)	532.596	0.9194	36348.82085	11.10
ZCO/VO (5 wt%)	Lattice O_L (O^{2-})	529.674	0.4596	174764.7516	0.84
ZCO/VO (5 wt%)	Defect/O_V (~531 eV)	530.915	1.2156	146787.1226	

ZCO/VO (5 wt%)	OH/Adsorbed (~532.5 eV)	532.587	0.3252	30.96726455	0.01

Table ST-5: Deconvolution results of the O 1s spectra for ZCO and ZCO/VO (5 wt%), showing the binding energy positions, peak widths (σ), integrated areas, and the relative fractions of lattice oxygen (O_L), oxygen vacancies/defective oxygen (O_V), and hydroxyl/adsorbed oxygen species. Compared with pristine ZCO, ZCO/VO exhibits a markedly higher O_V fraction, evidencing defect enrichment induced by VO incorporation and etching treatment. The generation of abundant oxygen vacancies is expected to enhance charge transfer and improve electrochemical activity.

Note S7. Electrochemical Analysis:

1. **Cyclic Voltammetry (CV):**

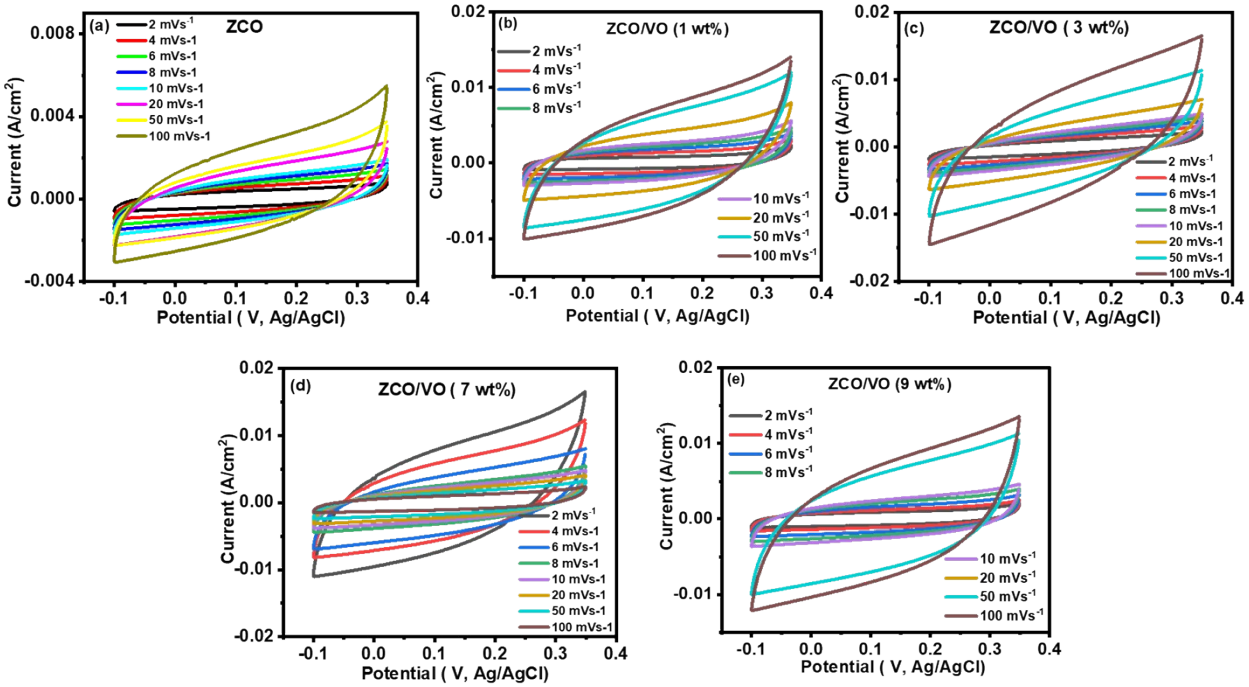

Fig. SF8: CV curves of (a) ZCO, (b) ZCO/VO (1 wt%), (c) ZCO/VO (3 wt%), (d) ZCO/VO (7 wt%), and (e) ZCO/VO (9 wt%) electrodes at different scan rates (2–100 mV s^{-1}) in a three-electrode system. The VO-modified electrodes exhibit enlarged CV areas relative to ZCO, confirming enhanced pseudocapacitive behavior, with ZCO/VO heterostructures showing improved redox reversibility and higher current response.

a. Calculation of Tafel slope:

The correlation between the anodic peak current and the scan rate was evaluated using these Equations [S3]**:**

$$i = av^b \tag{1}$$

$$\log(i) = \log(a) + b\log(v) \tag{2}$$

where i denotes the working electrode current (at V = 0), v is the scan rate, and b is the Tafel slope. The b-value was determined from the slope of the $\log(i)$ versus $\log(v)$ plot, which provides insights into the charge storage mechanism. A b-value of 0.5 indicates a diffusion-controlled process, while a value of 1.0 corresponds to a surface-controlled capacitive process. Intermediate b-values ($0.5 < b < 1.0$) reflect a mixed mechanism involving both faradaic and capacitive contributions. [S(4,5)]

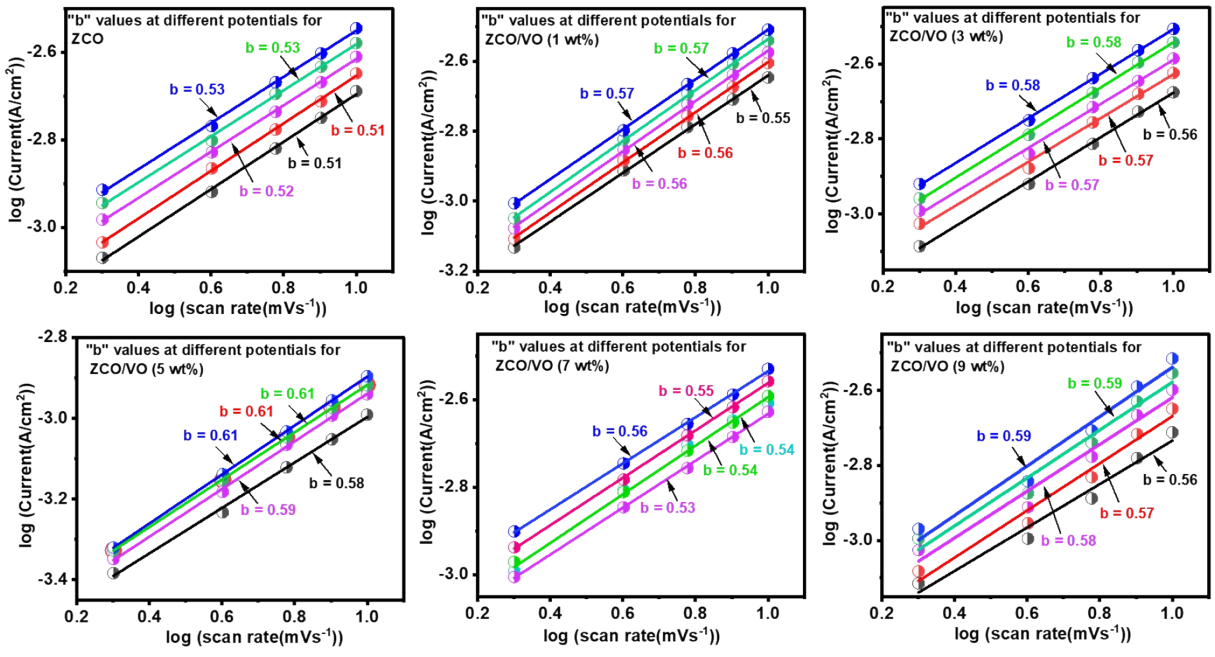

Fig. SF9: b-values were systematically determined at the anodic and cathodic peak potentials as well as at multiple potentials across the CV curves. The values (0.51–0.61) indicate predominantly pseudocapacitive-controlled behavior with minor diffusion contribution. The optimized 5 wt% sample exhibits relatively higher b-values, confirming enhanced charge storage kinetics and faster electrochemical response.

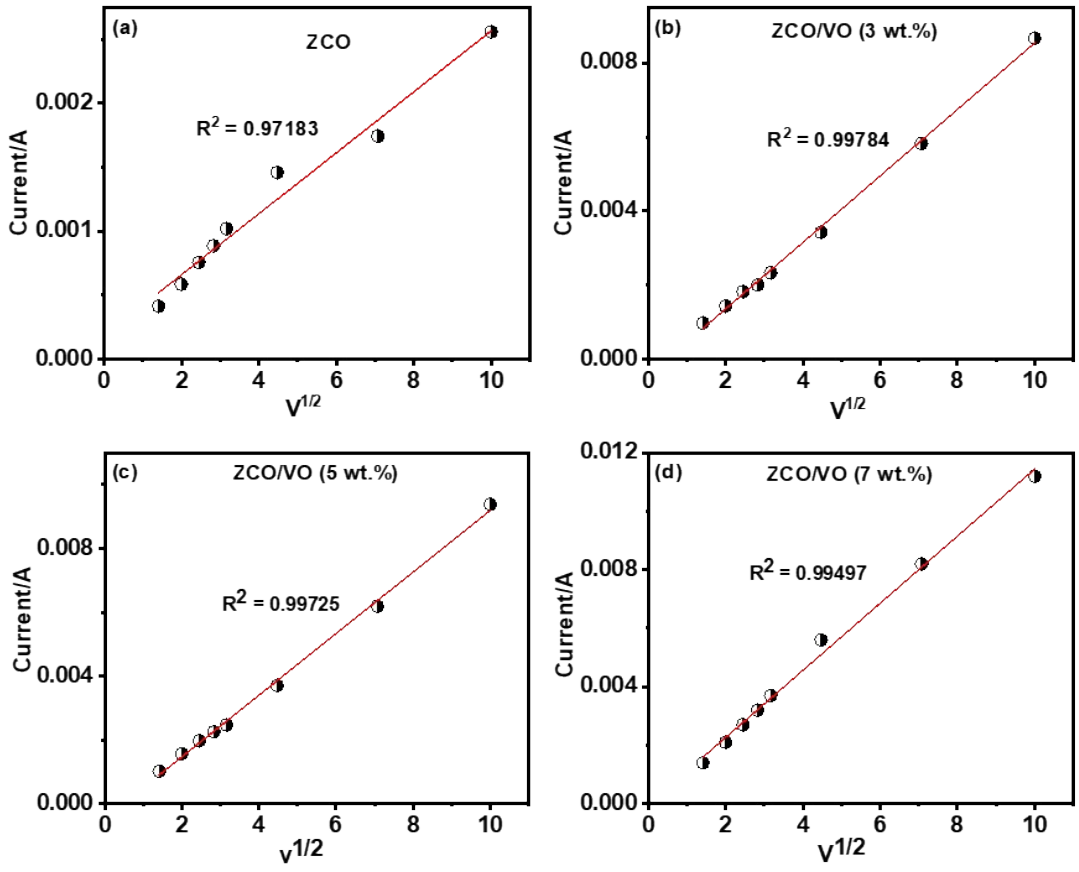

Fig. SF10: Linear fitting plots of $V^{1/2}$ vs current for (a) ZCO, (b) ZCO/VO (3 wt%), (c) ZCO/VO (5 wt%), and (d) ZCO/VO (7 wt%) electrodes. The excellent linear correlations (high R^2 values) confirm the reliability of the calculated b-value parameters and further validate the charge storage mechanism analysis.

b. Calculation of Capacitive and Diffusive contribution using the Dunn method:

To examine the reaction kinetics, the following equation is applied.[S6]

$$I(V) = k_1 v + k_2 v^{1/2} \tag{3}$$

$$\frac{I(V)}{v^{1/2}} = k_1 v^{1/2} + k_2 \tag{4}$$

I(V) is the current at V = 0, where $K_1 v$ and $K_1 v^{1/2}$ capacitive and diffusive contributions [S7]. From equation (4), the slope and intercept of the $\frac{I(V)}{v^{1/2}}$ vs $v^{1/2}$ plot yield K_1 and K_2. Therefore,

$$\text{Capacitive current} = \frac{k_1 v}{k_1 v + k_2 v^{1/2}} \times 100\% \tag{5}$$

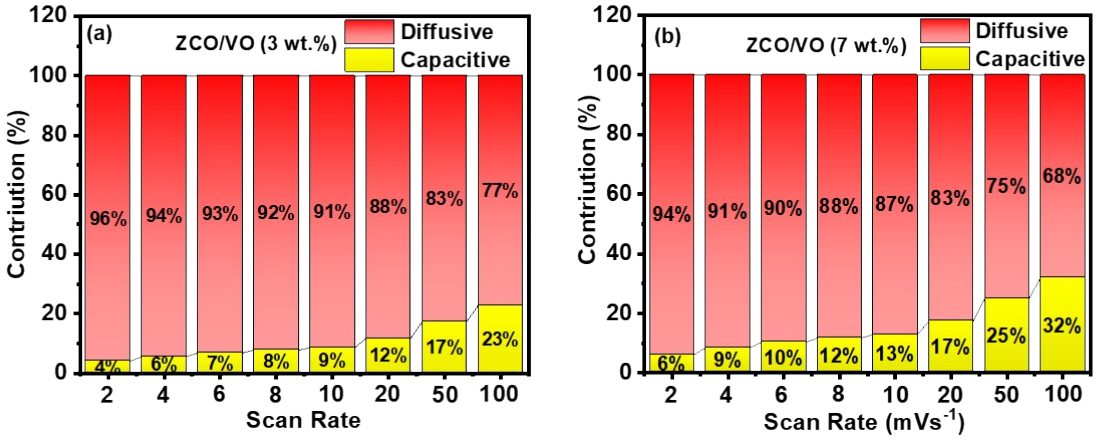

$$\text{Diffusive current} = \frac{k_2 v^{1/2}}{k_1 v + k_2 v^{1/2}} \times 100\% \qquad (6)$$

Fig. SF11: Capacitive and diffusive charge storage contributions at different scan rates for (a) ZCO/VO (3 wt%) and (b) ZCO/VO (7 wt%) electrodes. The capacitive contribution increases progressively with scan rate, while the diffusion-controlled contribution remains more dominant at lower scan rates. This analysis highlights the synergistic charge storage mechanism, where both surface-controlled capacitive and diffusion-controlled faradaic processes contribute to the overall electrochemical performance.

Table ST-6: Quantitative analysis of capacitive and diffusion-controlled contributions of the ZCO/VO nanocomposite at different scan rates using Dunn's.

	Scan rates (mV s^{-1})

Samples	Contribution (%)	2	4	6	8	10	20	50	100
ZCO	Capacitive	3	4	5	6	6	9	13	18
	Diffusive	97	96	95	94	94	91	87	82
ZCO/VO (3 wt%)	Capacitive	4	6	7	8	9	12	17	23
	Diffusive	96	94	93	92	91	88	83	77
ZCO/VO (5 wt%)	Capacitive	15	20	24	27	29	36	47	56
	Diffusive	85	80	76	73	71	64	53	44
ZCO/VO (7 wt%)	Capacitive	6	9	10	12	13	17	25	32
	Diffusive	94	91	90	88	87	83	75	68

c. Calculation of EDLC and Pseudocapacitance contribution using Trasatti method:

The Trasatti method was applied to distinguish the capacitance contributions from EDLC and pseudocapacitance using CV curves at different scan rates (2–10) mV s^{-1}. The total capacitance (C_T) was estimated by plotting $\frac{1}{C}$ versus $v^{1/2}$, where the y-intercept of the linear fit at low scan rates ($v \rightarrow 0$) corresponds to $\frac{1}{C_T}$, as given by Equation (7).[S8]

$$\frac{1}{C(v)} = const.v^{1/2} + \frac{1}{C_T} \quad (7)$$

At high scan rates ($v \rightarrow \infty$), ion access is limited to the outer surface, and the EDLC contribution (C_o) is obtained by plotting C versus $v^{-1/2}$, where the intercept of the linear fit gives C_o according to Equation (8):[S9]

$$C(v) = const.v^{-1/2} + C_o \quad (8)$$

The inner surface capacitance (C_i), corresponding to pseudocapacitance, is determined by subtracting C_o from C_T.

$$C_i = C_T - C_o \quad (9)$$

Assuming unrestricted linear ion diffusion, this approach quantifies the capacitive contributions in nanostructured electrodes using the specified equations.

$$C_i(\%) = \frac{C_i}{C_T} \times 100\% \tag{10}$$

$$C_o(\%) = \frac{C_o}{C_T} \times 100\% \tag{11}$$

2. Galvanostatic charge-discharge (GCD):

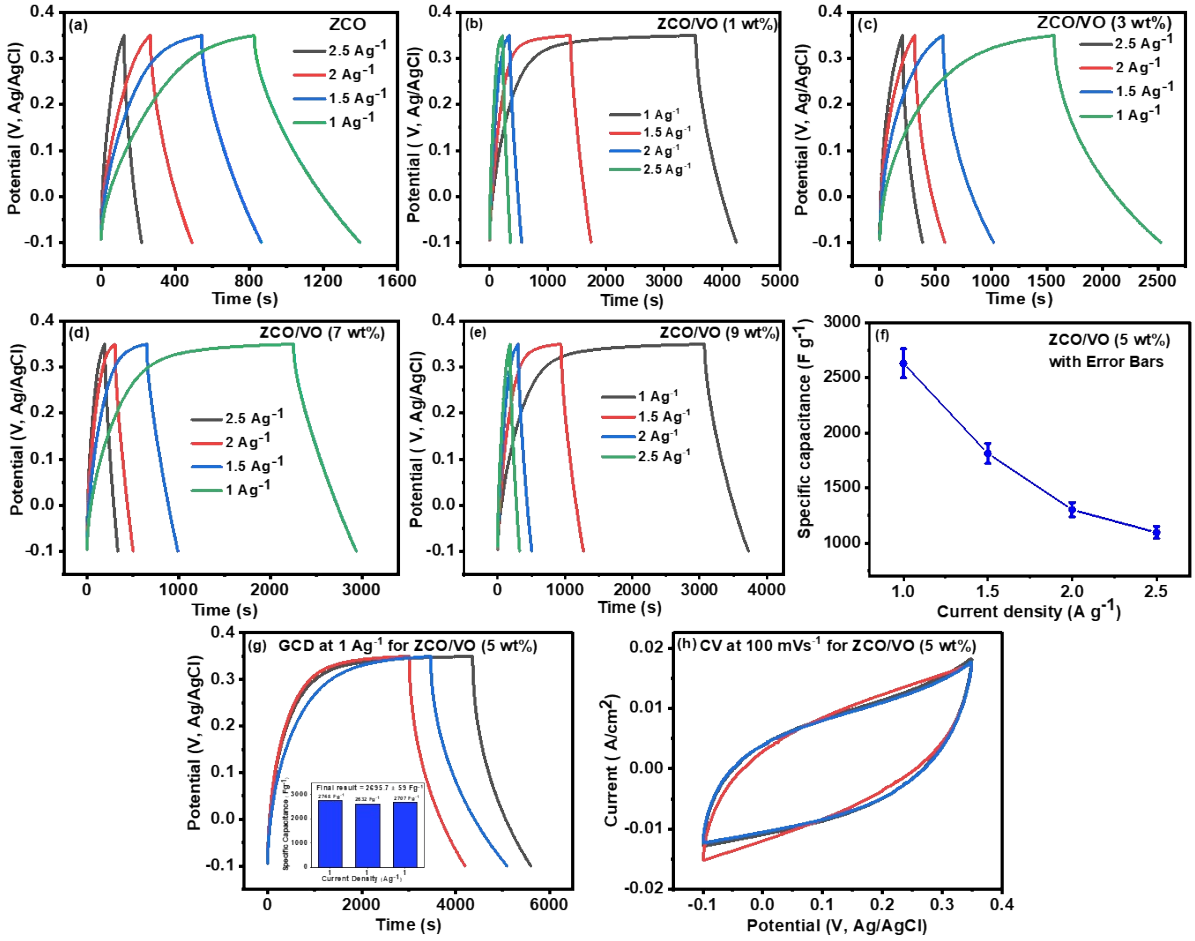

Fig. SF12: Galvanostatic charge–discharge (GCD) curves of (a) ZCO, (b) ZCO/VO (1 wt%), (c) ZCO/VO (3 wt%), (d) ZCO/VO (7 wt%), and (e) ZCO/VO (9 wt%) electrodes at various current densities (1, 1.5, 2, and 2.5 A g^{-1}). The ZCO/VO nanocomposites exhibit longer discharge times and enhanced capacity compared to pristine ZCO, highlighting the beneficial role of VO incorporation in improving charge storage capability and rate performance. (f) Rate capability of the ZCO/VO (5 wt%) electrode showing specific capacitance as a function of current density with corresponding error bars, indicating good rate performance and reproducibility. (g) GCD curves of the ZCO/VO (5 wt%) electrode recorded at repeated 1 A g^{-1} current densities, demonstrating quasi-symmetric profiles and good capacitive behavior; the inset shows the corresponding specific capacitance values. (h) CV curves of the ZCO/VO (5 wt%) electrode at repeated 100mV s^{-1} scan rates, exhibiting quasi-rectangular shapes with slight redox features, confirm the combined EDLC and pseudocapacitive charge storage mechanism.

Table ST-7: Specific capacitance (F g^{-1}) of ZCO and ZCO/VO heterostructures evaluated under various current densities.

Sample/Current Density (Ag^{-1})	1	1.5	2	2.5
ZCO	1270	1077	836	523
ZCO/VO (1 wt%)	1563	1187	943	739
ZCO/VO (3 wt%)	2136	1520	1209	1012
ZCO/VO (5 wt%)	2632	1813	1302	1095
ZCO/VO (7 wt%)	1529	1134	890	784
ZCO/VO (9 wt%)	1495	1116	898	805

The specific capacitance of ZCO and ZCO/VO nanocomposites was evaluated at various current densities to assess the influence of VO incorporation on charge-storage capability. As shown in Table ST-7, ZCO delivers a capacitance of 1270 F g^{-1} at 1 A g^{-1}, which gradually decreases to 523 F g^{-1} at 2.5 A g^{-1} due to the limited ion diffusion at high current loads. The introduction of VO markedly improves the electrochemical performance, with the capacitance increasing

systematically as the VO content rises from 1 to 5 wt%. In particular, the ZCO/VO (5 wt%) sample exhibits the highest capacitance, achieving 2632 F g^{-1} at 1 A g^{-1} and retaining 1095 F g^{-1} even at 2.5 A g^{-1}, reflecting its superior rate capability and the strong synergistic interaction between ZCO and VO. However, further increasing the VO content to 7 and 9 wt% leads to a decline in capacitance, likely due to excessive VO coverage that partially blocks active sites and hinders charge transport. Overall, the optimized 5 wt% VO loading provides the most favorable balance between redox activity and conductivity, resulting in the highest capacitive performance among all samples.

3. Electrochemical impedance spectroscopy (EIS):

Table ST-8: Equivalent circuit fitting parameters obtained for ZCO and ZCO/VO heterostructures with varying VO contents

Sample	Rs	CPE	Rct	C	W
ZCO	1.64	0.02969	11.81	0.03701	4.060
ZCO/VO (1 wt%)	2.49	0.07361	10.75	0.05389	3.355
ZCO/VO (3 wt%)	1.48	0.09612	4.09	0.07756	2.806
ZCO/VO (5 wt%)	0.97	0.01407	3.77	0.01273	2.433
ZCO/VO (7 wt%)	1.57	0.0893	22.44	0.04222	3.455
ZCO/VO (9 wt%)	2.34	0.0225	13.78	0.05371	3.287

The EIS fitting results show that ZCO exhibits R_S = 1.64 Ω, Rct = 11.81 Ω, and W = 4.060. With 1 wt% VO, Rs slightly increases (2.49 Ω) while Rct decreases to 10.75 Ω (W = 3.355). The 3 wt% sample shows further improvement with Rs = 1.48 Ω, Rct = 4.09 Ω, and W = 2.806. The 5

wt% composite delivers the best kinetics, showing the lowest Rs (0.97 Ω), lowest Rct (3.77 Ω), and reduced W (2.433). At higher VO contents (7 and 9 wt%), the resistances rise again, with Rs = 1.57/2.34 Ω, Rct = 22.44/13.78 Ω, and W = 3.455/3.287, indicating hindered charge-transfer and diffusion.

4. Cyclic stability:

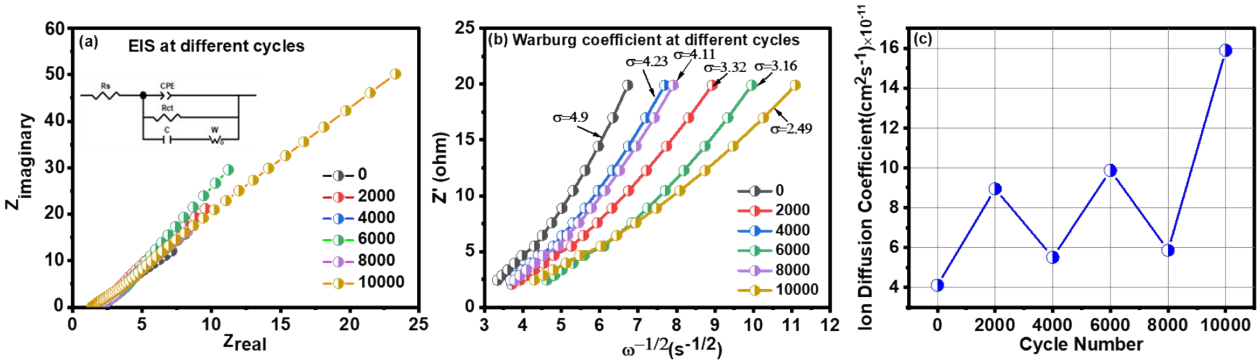

Fig. SF 13: (a) Nyquist plots of the electrode at different cycle numbers (0–10,000 cycles) with the fitted equivalent circuit (inset). (b) Enlarged high-frequency region showing the evolution of Rct during cycling. (c) Ion-diffusion coefficient as a function of cycle number, confirming progressively enhanced ion transport associated with the electrochemical activation process.

Table ST-9**.** Fitted EIS parameters (Rs, Rct, CPE, and W) and calculated ion-diffusion coefficients (Dion) for the electrode at different cycle numbers, highlighting the progressive improvement in charge-transfer kinetics and ion transport during electrochemical activation.

Cycle Numbers	Rs	CPE	Rct	C	W

0	0.97	0.01407	3.77	0.01273	2.433
2000	0.96	0.01018	3.28	0.01795	2.361
4000	0.98	0.01277	3.73	0.05746	2.403
6000	0.95	0.01762	3.48	0.01273	2.499
8000	0.99	0.01773	3.90	0.04222	2.391
10000	0.92	0.009	3.73	0.0103	2.317

Table ST-10: Electrochemical performance comparison between the as-fabricated ZCO/VO (5 wt%) nanocomposites and previously reported ZCO-based nanocomposites evaluated in a three-electrode system.

Electrode	Electrochemical cell configuration	Electrolyte	Potential Window (V)	Specific capacitance (Fg^{-1}) at Current density ($A\ g^{-1}$)	Capacitance retention (%) after cycles	Ref
$ZnCo_2O_4$/Ni-Co-S	Three	2 M KOH	0.5	1762.6 at 1	81.4 after 5000	S10
$ZnCo_2O_4$/PPy	Three	3 M KOH	0.5	1210 at 1	93.5 after 9000	S11
$ZnCo_2O_4$/MnO_2	Three	3 M KOH	0.6	2057 at 1	96.5 after 5000	S12
$ZnCo_2O_4$/rGO	Three	6 M KOH	0.42	1075.4 at 1	89.3 after 10000	S13
Porous $ZnCo_2O_4$	Three	2 M KOH	0.45	680 at 1	95.6 after 3000	S14
$NiCo_2O_4$/$ZnCo_2O_4$	Three	1 M KOH	0.55	1870 at 1	91 after 10000	S15
$ZnCo_2O_4$/CNT	Three	3 M KOH	0.6	1203.8 at 1	87 after 3000	S16
$ZnCo_2O_4$/$Ni_3V_2O_8$	Three	2 M KOH	0.5	1734 at 1	96 after 8000	S17
$ZnCo_2O_4$/N-GO PANI	Three	3 M KOH	0.5	720 at1.5	96.4 after 10000	S18
P-$ZnCo_2O_4$	Three	6 M KOH	0.5	1581.5 at 1		S19
ZnO/$ZnCo_2O_4$/NiO	Three	2 M KOH	0.5	1136.4 at 1	86.5 after 5000	S20
$NiCo_2O_4$/$ZnCo_2O_4$/ rGO	Three	1 M KOH	0.55	2176.4 at 1	93.8 after 5000	S21
ZCO/VO (5 wt%)	Three	3 M KOH	0.45	2632 at 1	111 after 1000	This work

Table ST-11: Comparison of the fitted EIS parameters (Rs, CPE, Rct, C, and W) for the ZCO/VO (5 wt%) electrode before and after 10,000 GCD cycles, obtained by fitting with Z-View.

Sample	Rs	CPE	Rct	C	W
Before-ZCO/VO (5 wt%)	0.97	0.014	3.77	0.0127	2.433
After-ZCO/VO (5 wt%)	0.92	0.009	3.73	0.0103	2.317

a. After XRD and SEM images:

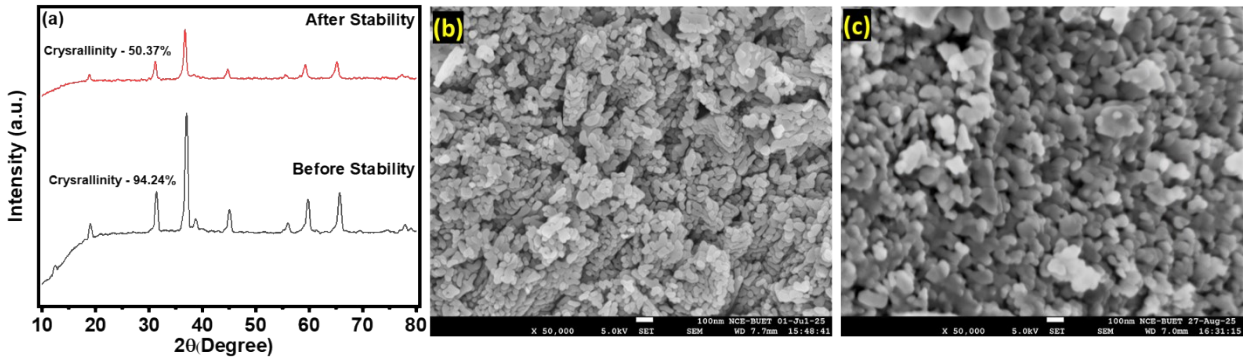

Fig. SF14: (a) XRD patterns of ZCO/VO (5 wt%) before and after 10,000 charge–discharge cycles, showing a decrease in crystallinity from 94% to 50% due to lattice distortion and partial amorphization during repeated ion insertion/extraction. (b) SEM image of ZCO/VO (5 wt%) before cycling, displaying compact and interconnected nanostructures. (c) SEM image after cycling, revealing a more porous and fragmented morphology. The reduction in crystallinity and morphological transformation creates additional electrochemically active sites, facilitating electrolyte penetration and thereby improving ion transport, which results in enhanced electrochemical performance after long-term cycling.

Table ST-12: Comparison of porosity parameters of the ZCO/VO (5 wt%) electrode before and after 10,000 GCD cycles, calculated using MATLAB

Sample	Porosity (%)	Average Pore Radius (nm)	Standard Deviation of Pore radius(nm)
Before-ZCO/VO (5 wt%)	6.43	10.149	11.651
After-ZCO/VO (5 wt%)	8.24	12.524	11.935

Note S8. Symmetric Two-electrode analysis:

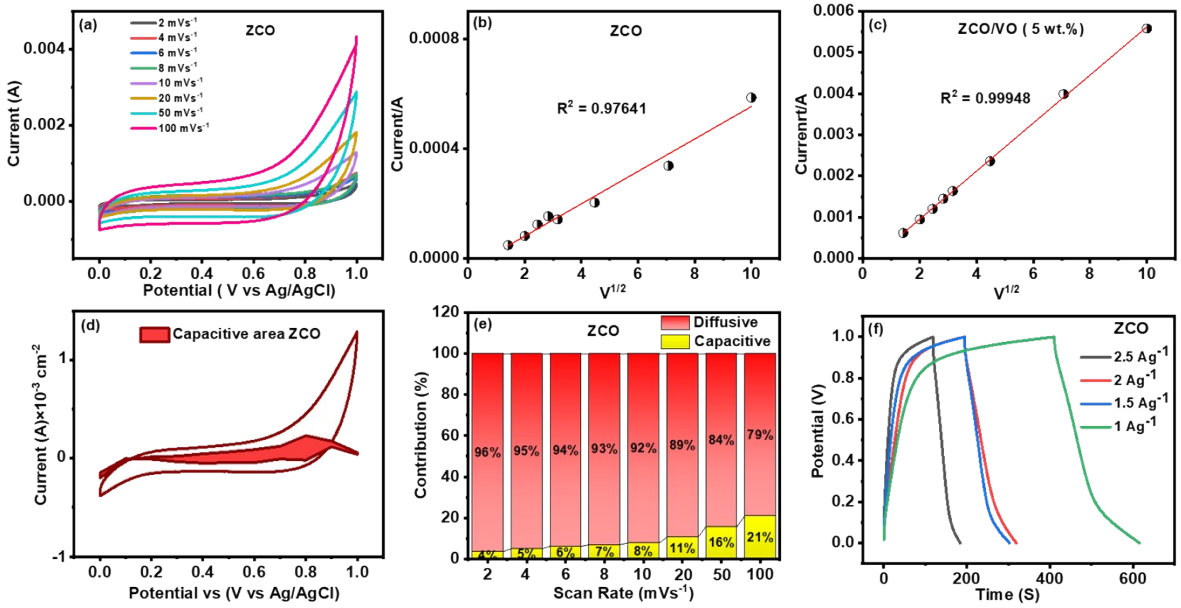

Fig. SF15: (a) CV curves of ZCO electrodes recorded at scan rates ranging from 2 to 100 mVs^{-1}. (b, c) Linear fitting of current response (i) versus the square root of scan rate ($v^{1/2}$) for ZCO and ZCO/VO (5 wt%), respectively, demonstrating the relationship between current and diffusion-controlled contributions. (d) Capacitive contribution analysis of ZCO from CV curves at different scan rates. (e) Quantitative comparison of capacitive and diffusion-controlled charge storage contributions in ZCO at various scan rates. (f) GCD profiles of ZCO at different current densities.

Table ST-13: Comparison of the specific capacitance, energy density, and power density of ZCO/VO (5 wt%) and pristine ZCO electrodes at different current densities.

Sample	Current Density (A g^{-1})	Specific Capacitance (F g^{-1})	Energy Density (W h kg^{-1})	Power Density (W kg^{-1})
ZCO/VO (5 wt%)	2.5	447	15.52	750
	2	498	17.3	625
	1.5	520	18.06	500
	1	1105	38.37	375
ZCO	2.5	223	7.75	750
	2	284	9.87	625
	1.5	334	11.6	500
	1	412	14.3	375

Table ST-14: EIS fitting parameters of ZCO and ZCO/VO (5 wt%) electrodes in a two-electrode symmetric configuration.

Sample	Rs	CPE	Rct	C	W
ZCO	2.23	0.06583	3.203	0.0013	8.672
ZCO/VO (5 wt%)	0.91	0.03825	3.08	0.0023	9.584

Note S9. Asymmetric Two-electrode analysis:

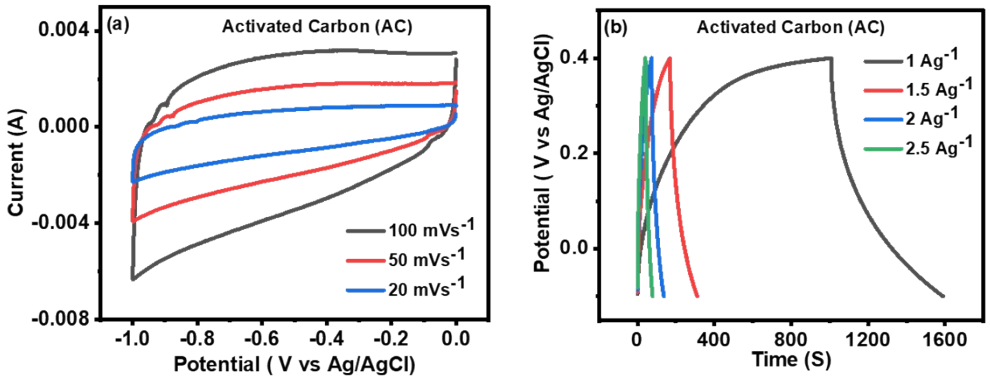

Fig. SF16: (a) CV curves of the activated carbon electrode recorded at different scan rates, exhibiting nearly rectangular profiles indicative of ideal electric double-layer capacitive behavior. (b) GCD profiles of activated carbon at various current densities, showing symmetric charge–discharge characteristics with minimal IR drop, further confirming its excellent reversibility and capacitive performance.

Table ST-15: Equivalent circuit fitting results showing Rs, Rct, ZW, and Cp values for the asymmetric two-electrode setup.

Sample	**Rs**	**CPE**	**Rct**	**C**	**W**
ZCO/VO (5 wt%)	0.896	0.060	2.203	0.08596	3.98

Table ST-16: Electrochemical performance of the ZCO/VO (5 wt%) electrode in a two-electrode asymmetric configuration, showing the variation of specific capacitance, energy density, and power density with respect to current density.

Sample	Current Density ($A\ g^{-1}$)	Specific Capacitance ($F\ g^{-1}$)	Energy Density ($W\ h\ kg^{-1}$)	Power Density ($W\ kg^{-1}$)
ZCO/VO (5 wt%)	6	151	38.25	4050
	5	170	43	3375
	4	178	45	2700
	3	196	49.5	2025
	2	293	75	1350
	1	403	102	675

The ZCO/VO (5 wt%) device exhibits a clear dependence of electrochemical performance on current density. At lower current density (1 A g^{-1}), the electrode delivers the highest specific capacitance of 403 F g^{-1} with an energy density of 102 W h kg^{-1} at a power density of 675 W kg^{-1}. With increasing current density, both the capacitance and energy density gradually decrease due to limited ion diffusion and reduced redox activity, while the power density increases correspondingly, reaching 4050 W kg^{-1} at 6 A g^{-1}. This trade-off highlights the excellent rate capability and balanced energy–power characteristics of the ZCO/VO (5 wt%) electrode.

Note S10. Electrochemical Performance of Two-Electrode Devices:

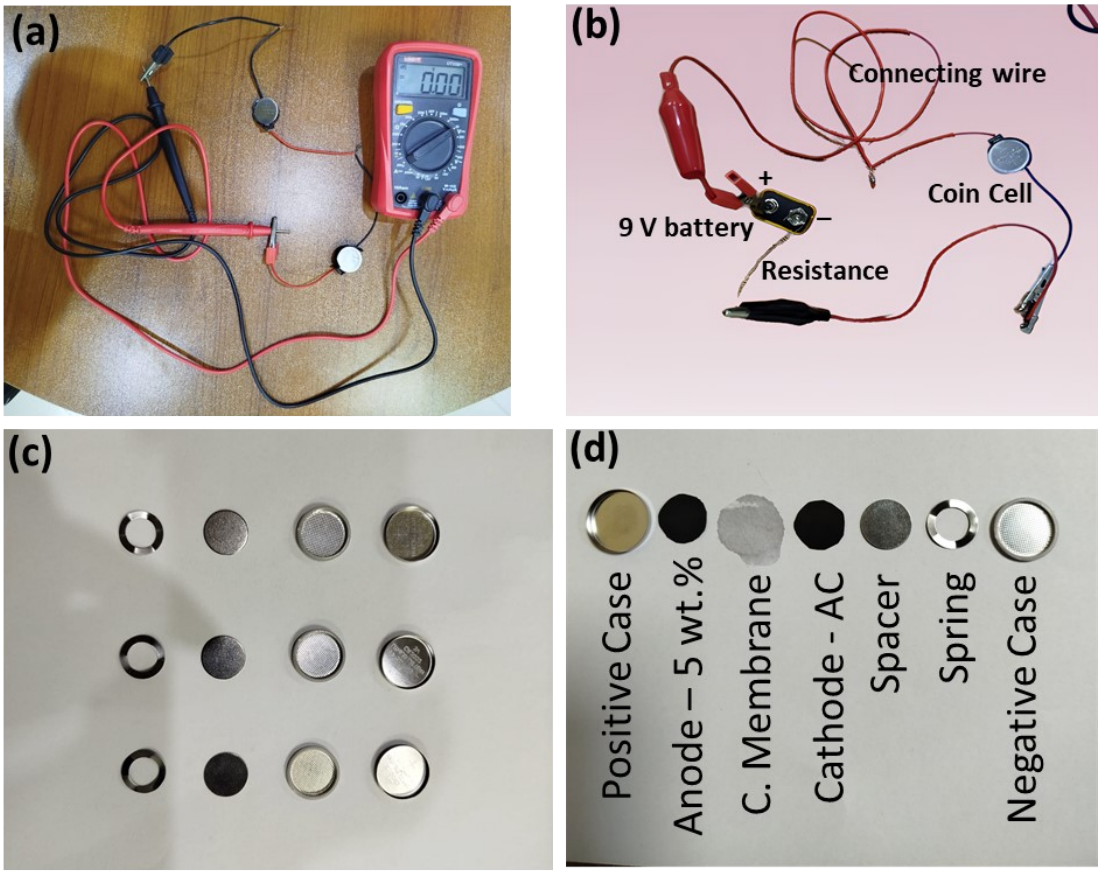

Fig. SF17: (a) Photograph of the fabricated coin cell showing negligible open-circuit voltage before charging. (b) Schematic representation of the charging process, where the coin cell is connected to a 9 V battery via an external resistor to initiate electrochemical activation. (c) Optical images of the disassembled coin cell illustrating its structural components. (d) Systematic arrangement of the constituent parts employed in coin cell fabrication, including the positive case, active material-coated anode (5 wt%), cellulose membrane separator, activated carbon cathode, metallic spacer, spring, and negative case, ensuring proper stacking and stable electrochemical performance.

Notes and References:

S1. A. Rabbani and S. Salehi, *J. Nat. Gas Sci. Eng.*, 2017, *42*, 157–168.
S2. C. P. Ezeakacha, A. Rabbani, S. Salehi, and A. Ghalambor, *SPE Int. Conf. Exhib. Formation Damage Control*, Society of Petroleum Engineers, 2018.
S3. Q. Mahmood, S. K. Park, K. D. Kwon, S.-J. Chang, J.-Y. Hong, G. Shen, Y. M. Jung, T. J. Park, S. W. Khang, W. S. Kim *et al.*, *Adv. Energy Mater.*, 2016**,** *6*, 1501115.
S4. H. B. Aiyappa, J. Masa, C. Andronescu, M. Muhler, R. A. Fischer, and W. Schuhmann, *Small Methods*, 2019, *3*, 1800415.
S5. H. Wang, S. Zhang, and C. Deng, *ACS Appl. Mater. Interfaces*, 2019, *11*, 35796–35808.
S6. J. Wang, J. Polleux, J. Lim and B. Dunn, *J. Phys. Chem. C*, 2007, *111*, 14925–14931.
S7. R. Wang, S. Wang, X. Peng, Y. Zhang, D. Jin, P. K. Chu, and L. Zhang, *ACS Appl.Mater. Interfaces*, 2017, 9, 32745–32755.
S8. S. Ardizzone, G. Fregonara, and S. P. Trasatti, *Electrochim. Acta*, 1990, *35*, 263–267.
S9. Z.H. Huang, T.-Y. Liu, Y. Song, Y. Li, and X.-X. Liu, *Nanoscale*, 2017, *9*, 13119–13127.
S10. H. Xuan, H. Li, J. Gao, Y. Guan, Z. Xie, X. Liang and Y. Wu, *Appl. Surf. Sci.*, 2020, *513*, 145893.
S11. X. Liu, Q. Li, Y. Qin and Y. Jiang, *RSC Adv.*, 2020, *10*, 28324–28331.
S12. V. S. Kumbhar and D. H. Kim, *Electrochim. Acta*, 2018, *271*, 284–296.
S13. M. Yan, F. Jiang, Y. Liu, L. Sun, H. Bai, F. Zhu and W. Shi, *Colloids Surf., A*, 2021, *612*, 125902.
S14. J. Qi, J. Mao, A. Zhang, L. Jiang, Y. Sui, Y. He and X. Zhang, *J. Mater. Sci.*, 2018, *53*, 16074–16085.
S15. A. J. C. Mary, C. I. Sathish, P. S. M. Kumar, A. Vinu and A. C. Bose, *Electrochim. Acta*, 2020, *342*, 136062.
S16. L. Wu, L. Sun, X. Li, Q. Zhang, H. Si, Y. Zhang, and Y. Zhang, *Appl. Surf. Sci.*, 2020, *506*, 144964.
S17. Y. Huang, X. Feng, C. Li, Y. Li, X. Chen, X. Gao, and P. Liu, *Ceram. Int.*, 2019, *45*, 15451–15457.
S18. A. Kathalingam, S. Ramesh, H. M. Yadav, J. H. Choi, H. S. Kim and H. S. Kim, *J. Alloys Compd.*, 2020, *830*, 154734.
S19. X. Wei, H. Wu and L. Li, *J. Alloys Compd.*, 2021, *861*, 158544.
S20. C. Huang, C. Hao, Z. Ye, S. Zhou, X. Wang, L. Zhu and J. Wu, *Nanoscale*, 2019, *11*, 10114–10128.
S21. A. J. C. Mary, C. I. Sathish, A. Vinu, and A. C. Bose, *Energy Fuels*, 2020, *34*, 10131–10141.